Electronic Supplementary Information (ESI) for Chemical Communications. This journal is (c) The Royal Society of Chemistry 2025.
Electronic Supplementary Information (ESI)

Designing a ternary $NiS_2/CoS_2@SnS_2$ nanocube as secondary battery anode displaying excellent capacity and stability

Huizi Songtian[a,#], Fengming Ma[b,#], Fan Zhou[c,#], Keke Wang[a], Fan Bu[a], Xulai Yang[c], Tianli Han[a,*], Jinjin Li[c,d,*] and Jinyun Liu[a,*]

Experimental

Materials

All chemicals, including $Co(NO_3)_2·6H_2O$, $Ni(NO_3)_2·6H_2O$, $SnCl_4·5H_2O$, thioacetamide (TAA), trisodium citrate trihydrate ($C_6H_5Na_3O_7·3H_2O$), $K_3[Co(CN)_6]$, anhydrous ethanol and sulfur powder, were of analytical grade and used without further purification.

Synthesis of NiCo-PBA

Typically, 11.25 mmol of $C_6H_5Na_3O_7·3H_2O$ and 7.5 mmol of $Ni(NO_3)_2·6H_2O$ were dissolved in 250 mL of deionized water under vigorous stirring to form Solution A. Separately, 4.99 mmol of $K_3[Co(CN)_6]$ was dissolved in 250 mL of deionized water under vigorous stirring to form Solution B. Solution B was then rapidly poured into Solution A, and the mixture was stirred for 10 minutes, followed by aging at room temperature for 24 hours. Subsequently, the product was washed and centrifuged to obtain the precursor of the nanocubes.

Synthesis of NiS_2/CoS_2

The precursor and sulfur powders were placed in separated ceramic boats at a weight ratio of 1:10, and calcined at 400 °C for 2 hours under an argon atmosphere, with a heating rate of 2 °C min^{-1}.

Synthesis of $NiS_2/CoS_2@SnS_2$

0.05 g of NiS_2/CoS_2 and 0.05 g of TAA were dispersed in 20 mL of anhydrous

ethanol and ultrasonicated for 10 minutes to form Solution A. Then, 0.10 g of $SnCl_4 \cdot 5H_2O$ was dispersed in 15 mL of anhydrous ethanol under stirring to form Solution B. Solution B was added to Solution A, and the mixture was stirred for 10 minutes. A hydrothermal reaction was subsequently conducted at 160 °C for 12 hours. At last, the sample was washed with water and ethanol, and dried at 60 °C for 8 hours, yielding the final product.

Characterizations

The phase of the samples was analyzed by using X-ray diffraction (XRD, Rigaku SmartLab, Cu target). Morphology and structure were examined by using field-emission scanning electron microscopy (SEM, Hitachi S4800), and transmission electron microscopy (TEM, Hitachi HT-7700). High-resolution TEM (HRTEM, JEOL JEM-2010) was employed to observe lattice fringes. Additional characterizations included X-ray photoelectron spectroscopy (XPS, Thermo Scientific), thermogravimetric analysis (TGA, PerkinElmer STA 6000), Brunauer-Emmett-Teller (BET) surface area measurements. Metal element content was measured by using an inductively coupled plasma spectrometry (ICP, Agilent 720ES), *In situ* XRD was conducted using a Rigaku SmartLab SE XRD system coupled with a battery testing system. *In situ* Raman was conducted using Raman spectroscopy (Renishaw in Via) equipped with an electrochemical workstation (CHI660e).

Electrochemical tests

A uniform slurry was prepared by dispersing the active material, conductive carbon black, and polyvinylidene fluoride (PVDF) binder in a weight ratio of 8:1:1 in N-methyl-2-pyrrolidone (NMP). The slurry was coated onto copper foil and dried at 80°C in a vacuum oven for 24 hours. The foil was then cut into 1.2 mm diameter discs with a mass loading of 1.0 mg cm^{-2}. Sodium metal was used as the counter electrode, and a glass fiber membrane served as the separator. The electrolyte consisted of 1 M $NaPF_6$ dissolved in diethylene glycol dimethyl ether. Battery assembly was conducted in an Ar-filled glovebox. Galvanostatic charge-discharge (GCD) tests were performed on a Neware battery tester, while cyclic voltammetry (CV) and electrochemical impedance spectroscopy (EIS) measurements were carried out on a CHI660e

electrochemical workstation. To assemble the full cells, the $Na_3V_2(PO_4)_3$ (NVP) cathode was prepared by making a slurry composing of NVP, acetylene black and PVDF in a weight ratio of 8:1:1, and casting it onto aluminum foil. The foil was then cut into 1.2 cm diameter discs. The N/P ratio was about 1.07. The electrolyte consisted of 1 M $NaPF_6$ dissolved in diethylene glycol dimethyl ether.

Computational method

Density functional theory calculations were carried out to investigate the properties of $NiS_2/CoS_2@SnS_2$ heterostructure using the Vienna ab initio Simulation Package (VASP) with the projector augmented wave (PAW) method. The exchange and correlation functionals were treated by using the Generalized Gradient Approximation (GGA) in the scheme of Perdew-Burke-Ernzerhof (PBE). The cutoff energy was set at 520 eV for the plane-wave extension of the wave function. The convergence criteria of geometric optimization were set to 10−5 eV in energy and 0.02 eV Å−1 in force. The 4×2×1 Monkhorst-Pack k-point meshes were used for geometric optimization. To properly evaluate the weak interaction at the interface, the DFT-D3 method with Becke-Jonson damping was chosen to deal with the van der Waals (vdW) correction. A vacuum layer of at least 20 Å was used to avoid the interactions between the periodic images in the Z-axis direction.

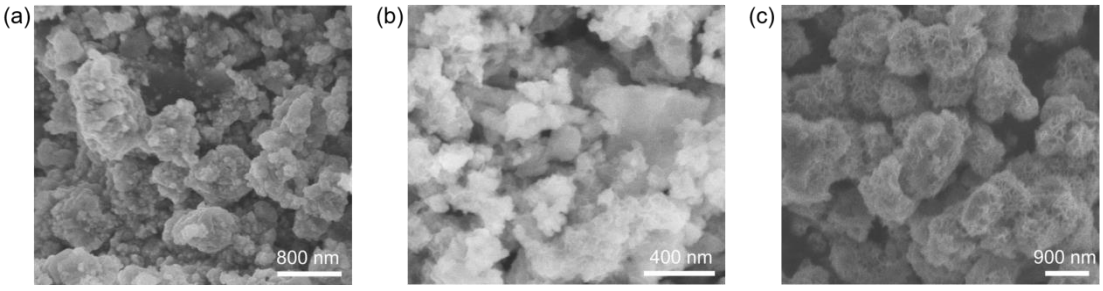

Fig. S1 SEM images of samples prepared by using concentration ratios of NiS_2/CoS_2:$SnCl_4$=1:1, 1:3, and 1:4.

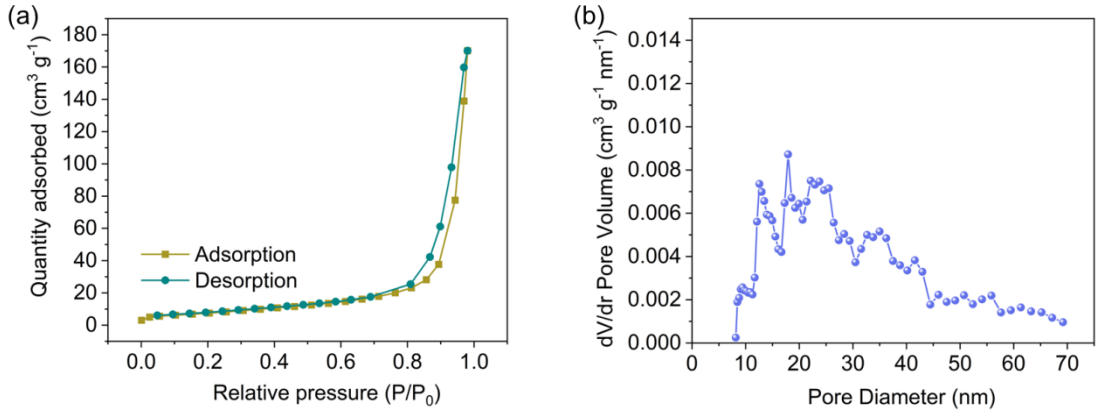

Fig. S2 (a) Nitrogen adsorption-desorption isotherms of NiS_2/CoS_2 and (b) pore-size distribution.

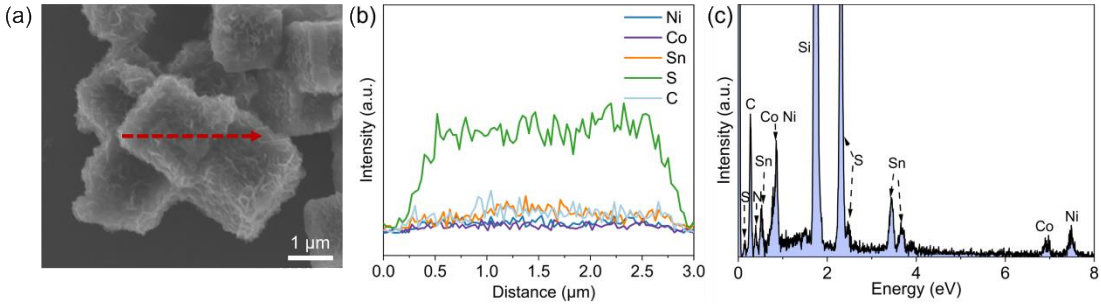

Fig. S3 (a) SEM image, (b) line-scanning curves and (c) EDS spectrum of $NiS_2/CoS_2@SnS_2$.

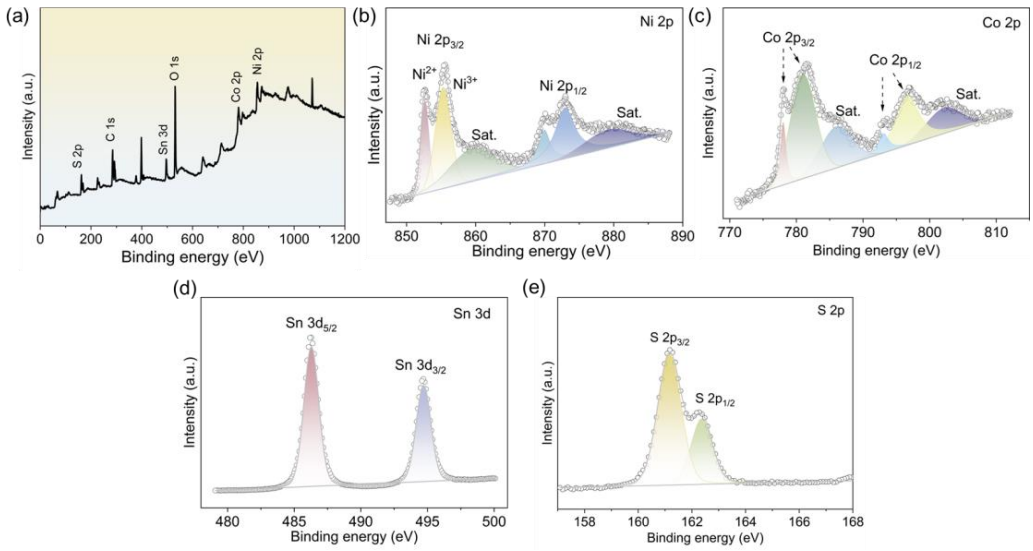

Fig. S4 (a) XPS survey spectrum, (b) Ni 2p, (c) Co 2p (d) Sn 3d, (e) S 2p of $NiS_2/CoS_2@SnS_2$.

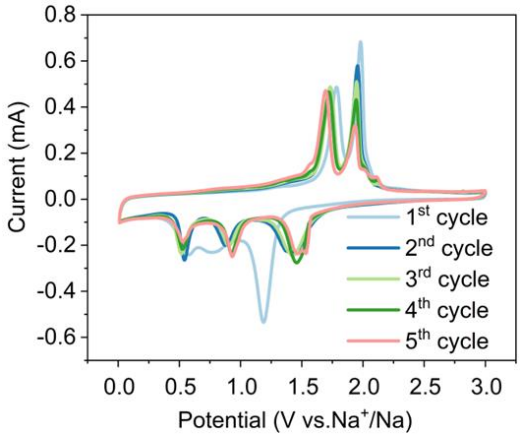

Fig. S5 CV profiles of the NiS_2/CoS_2 anode at 0.1 mV s^{-1}.

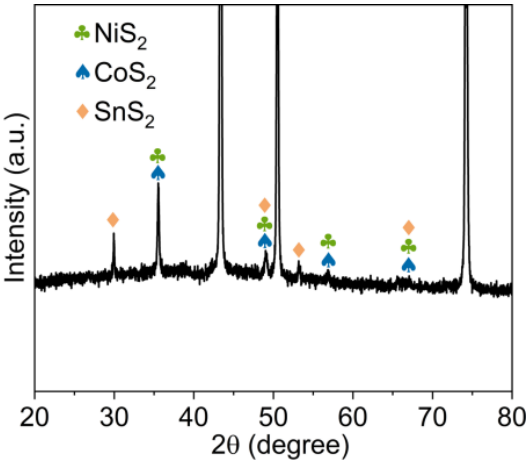

Fig. S6 XRD pattern of $NiS_2/CoS_2@SnS_2$ after 50 cycles at 0.5 Ag^{-1}.

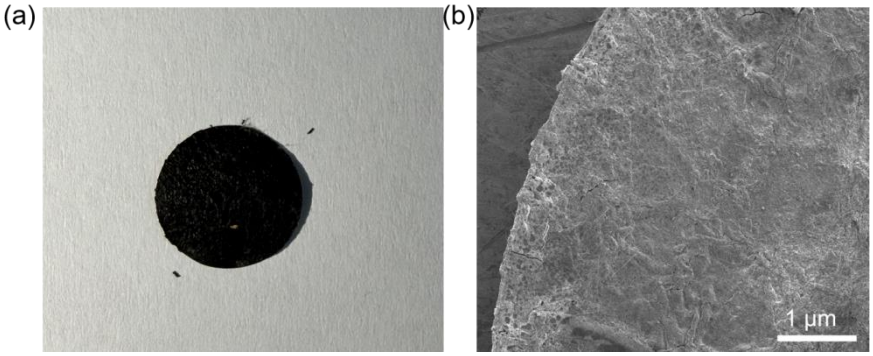

Fig. S7 (a) Photo and (b) SEM images of the $NiS_2/CoS_2@SnS_2$ electrode after 50 cycles at a current density of 1 A g^{-1}.

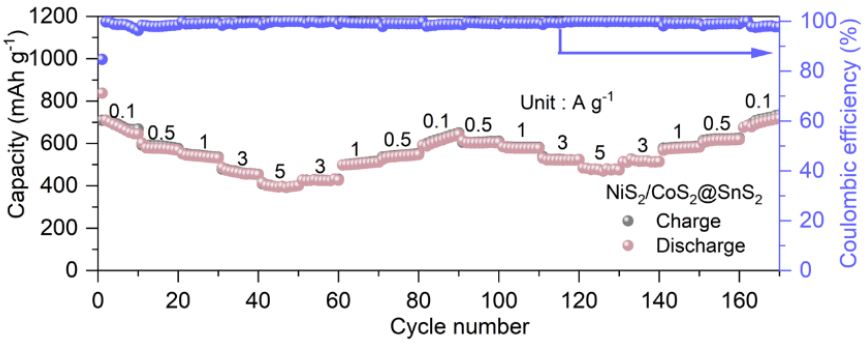

Fig. S8 Rate-performance of $NiS_2/CoS_2@SnS_2$.

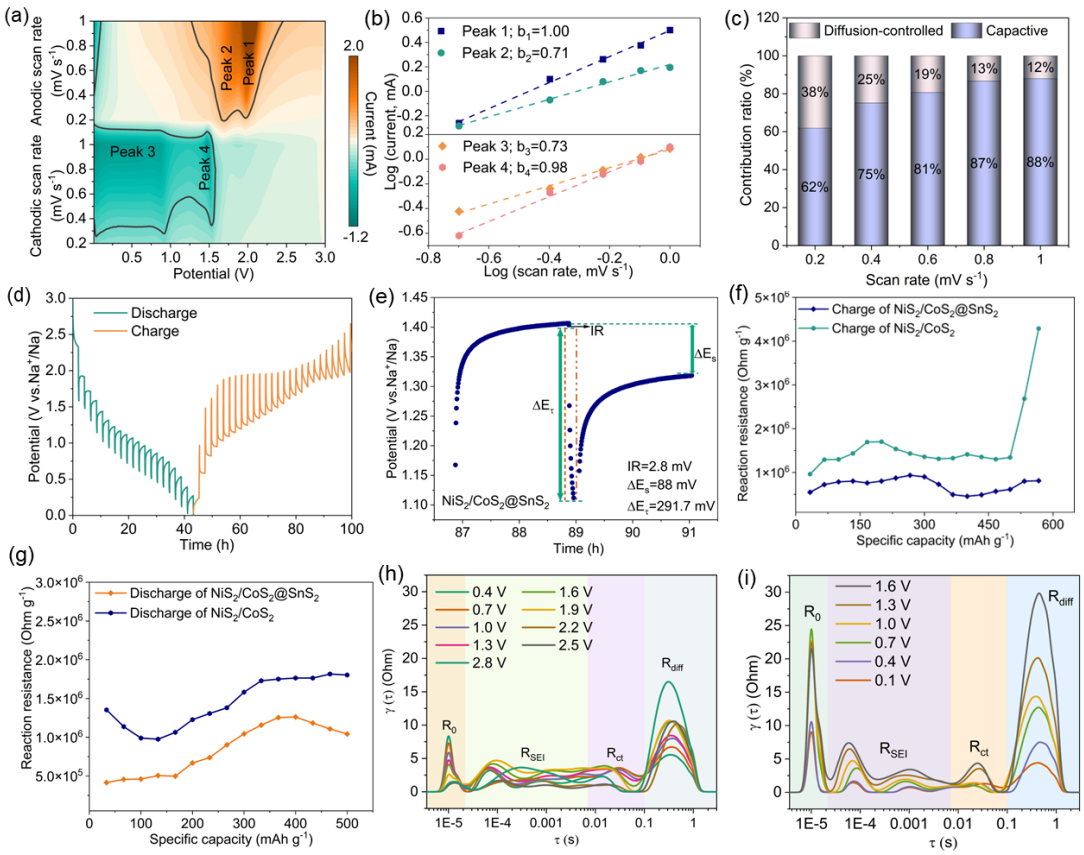

Fig. S9 (a) CV strength map, and (b) the log (*i*) vs. log (*v*) of the oxidization and reduction peaks, (c) ratio of pseudo-capacitive contribution, (d) GITT time-potential distributions, and (e) illustration of dEs, dEτ and IR drop of $NiS_2/CoS_2@SnS_2$. Reaction resistances of $NiS_2/CoS_2@SnS_2$ and NiS_2/CoS_2 during (f) charge and (g) discharge. Distribution of relaxation times (DRT) contour pattern corresponding to EIS spectra from (h) 0.4 to 2.8 V and (i) 1.6 to 0.1 V for the first cycle of $NiS_2/CoS_2@SnS_2$

Fig. S9 displays the CV strength map, revealing that the peak positions in the CV curves remain unchanged as the rate increases, indicating low polarization and excellent

reversibility. For comparison, the CV of the NiS_2/CoS_2 sample was also tested (Fig. S10). The scanning rate (v) and peak current (i) follow $i = av^b$. As shown in Fig. S9b, b values for peaks 1 to 4 of $NiS_2/CoS_2@SnS_2$ are 1.0, 0.71, 0.73, and 0.98, respectively, indicating Na-storage is dominated by capacitive behavior.[1] While b values of NiS_2/CoS_2 are presented in Fig. S11. Additionally, capacitive contribution is quantified using the equations $i = k_1v + k_2v^{0.5}$ and $i/v^{0.5} = k_1v^{0.5} + k_2$. Fig. S9c illustrates that capacitive contribution increases from 62% to 88% as rate rises from 0.2 to 1.0 mV s^{-1}, further confirming the pseudocapacitive mechanism. Galvanostatic intermittent titration technique (GITT) was employed to evaluate *in situ* internal resistance during charge-discharge (Fig. S9d). Fig. S9f and g demonstrates that internal resistance of $NiS_2/CoS_2@SnS_2$ is consistently lower than that of NiS_2/CoS_2, indicating reduced energy barriers and superior conductivity for the ternary composite. As shown in Fig. S9e, the IR drop and dEτ of $NiS_2/CoS_2@SnS_2$ are smaller than those of NiS_2/CoS_2 (Fig. S12). Relaxation time distribution (DRT) analysis was performed to study the of resistance evolution. During discharge (Fig. S9i), $NiS_2/CoS_2@SnS_2$ forms conductive Na-bonded metal sulfides as Na^+ ions intercalate, leading to a continuous decrease in charge transfer resistance (R_{ct}). At 0.1 V, the formation of highly conductive metallic Ni, Co, and Sn reduces R_{ct} further to a minimum value. Concurrently, the diffusion energy barrier decreases, resulting in a gradual reduction in diffusion resistance (R_{diff}). In contrast, both R_{ct} and R_{diff} increase progressively during the subsequent charging process (Fig. S9h), while they decrease in discharge (Fig. S9i), which is ascribed to the transport of Na^+ ions.[2,3] These findings highlight the enhanced electrochemical kinetics and reduced impedance of the $NiS_2/CoS_2@SnS_2$ anode. Furthermore, the electrochemical impedance spectroscopy (EIS) spectra of $NiS_2/CoS_2@SnS_2$ and NiS_2/CoS_2 are shown in Fig. S13. The fitted equivalent circuit reveals that the R_{ct} of $NiS_2/CoS_2@SnS_2$ (38.2 Ω) is significantly lower than that of NiS_2/CoS_2 (65.3 Ω).

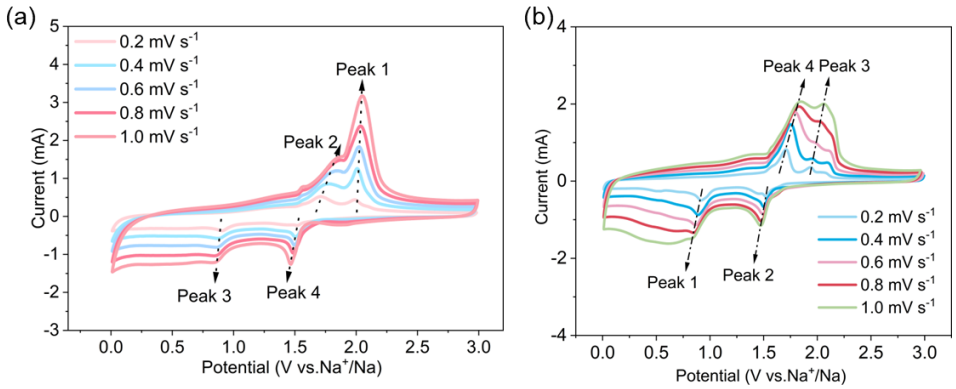

Fig. S10 CV curves of (a) $NiS_2/CoS_2@SnS_2$, and (b) NiS_2/CoS_2 at scanning rates from 0.2 to 1.0 mV s^{-1}.

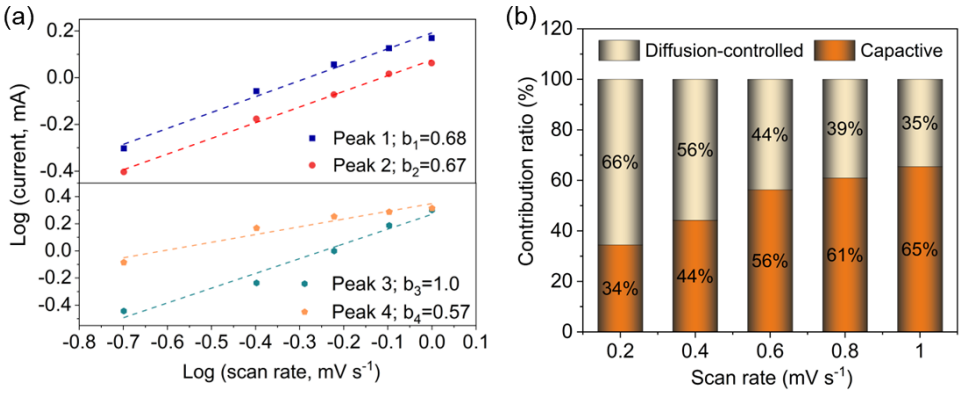

Fig. S11 (a) The log (i) vs. log (v) of oxidization and reduction peaks of NiS_2/CoS_2, (b) Ratios of pseudo-capacitive contribution of NiS_2/CoS_2.

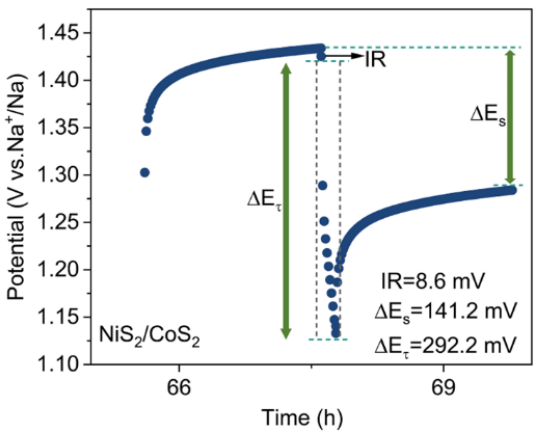

Fig. S12 Illustration for dEs, dEτ and IR drop of NiS_2/CoS_2.

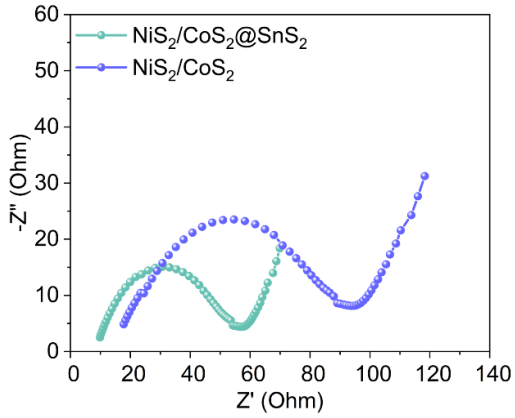

Fig. S13 EIS spectra of fresh cells based on $NiS_2/CoS_2@SnS_2$ and NiS_2/CoS_2.

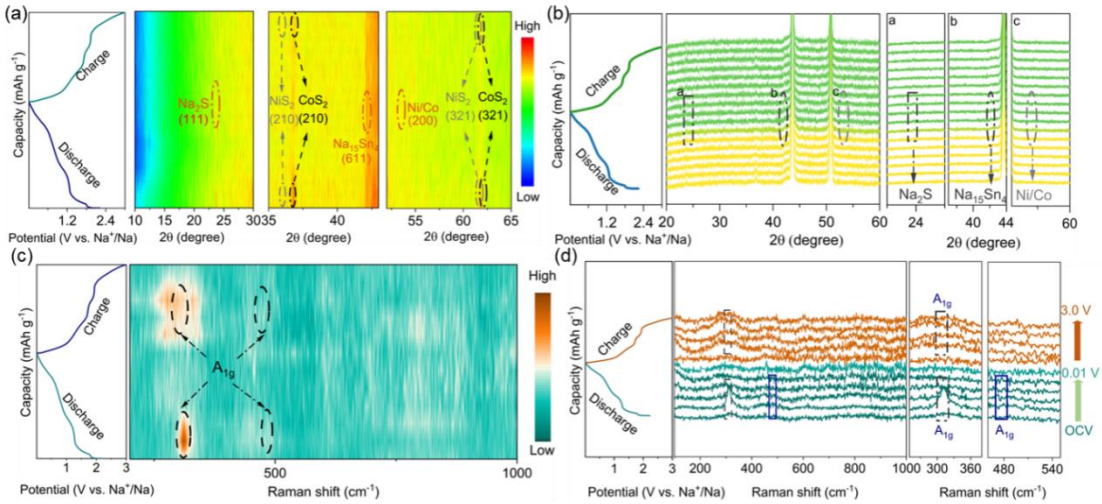

Fig. S14 (a) Contour plots of *in situ* XRD pattern of $NiS_2/CoS_2@SnS_2$ upon charge and discharge. (b) XRD patterns at different potentials. (c) Contour plots of *in situ* Raman spectra of $NiS_2/CoS_2@SnS_2$ anode during charge-discharge. (d) Raman spectra at a set of potentials.

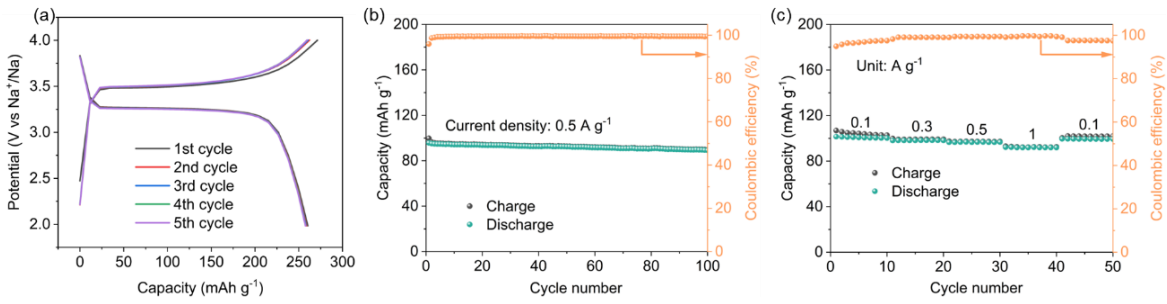

Fig. S15 (a) GCD curves, (b) electrochemical performance at 0.5 A g^{-1}, (c) rate-performance of $Na_3V_2(PO_4)_3$ cathode.

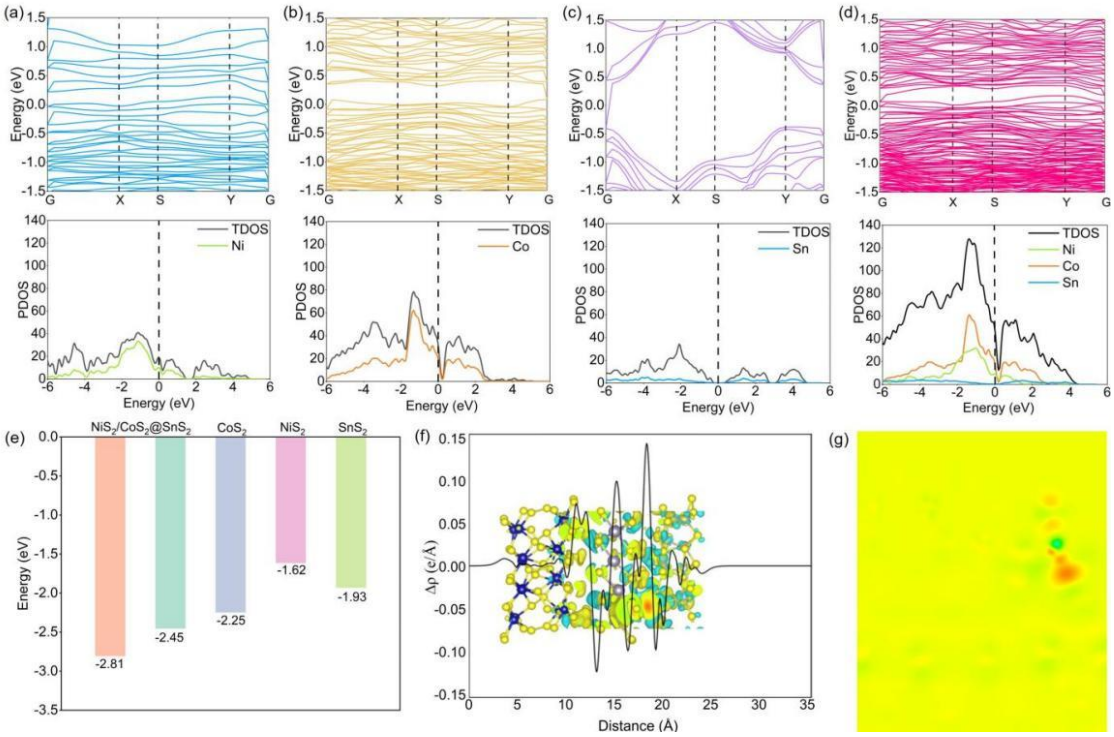

Fig. S16 Band structures and DOS of (a) NiS_2 (b) CoS_2 (c) SnS_2 and (d) $NiS_2/CoS_2@SnS_2$, where the Fermi levels are set to zero. (e) The adsorption energies of $NiS_2/CoS_2@SnS_2$, CoS_2, NiS_2 and SnS_2 towards Na^+ ions. (f) Charge density difference and planar-averaged charge density difference of $NiS_2/CoS_2@SnS_2$. Yellow and cyan represent charge accumulation and depletion, respectively. (g) Corresponding slice of charge density difference.

Table S1. Comparison on electrochemical performance of Na-ion battery anodes.

Anode materials	Current density ($A\ g^{-1}$)	Capacity ($mAh\ g^{-1}$)	Cycle number	Refs.
$NiS_2/CoS_2@SnS_2$	2.0	475.6	1000	This work
nanocubes	5.0	223.4	2500	
SnS_2/NiS_2@CC nanosheets	2.0	343.2	100	4
Hollow SnS_2/NiS_2@HCNFs nanofibers	2.0	315	1000	5
Microsphere shape CoNiZnS/C	2.0	410.7	960	6
Porous hollow polyhedron MnS-(ZnCo)S/N-C	2.0	316	400	7
SnS/FeS/Fe_3N/NC NSs nanosheets	2.0	473.6	600	8
Co_4S_3/Co_9S_8/ZnS microflowers	0.1	444	600	9
SnS@FeS/C	1.0	360	1000	10
In_2S_3/CoS_2 nanocubes	2.0	464.1	600	11

References

1 1 Y. J. Liu, Y. Gao, Y. Zhang, L. H. Xu, J. X. Chen, X. Hu, Z. H. Wen, *Angew. Chem. Int. Ed.*, 2025, **64**, e202505469.

2 K. Yang, Z. Y. Wang, Z. Q. Li, H. T. Ma, X. D. Geng, W. C. Li, N. Zhu, *Chem. Eng. J.*, 2025, **517**, 164448.

3 S. N. Sampathkumar, P. Aubin, K. Couturier, X. F. Sun, B. R. Sudireddy, S. Diethelm, M. Perez-Fortes, J. Van Herle, *Int. J. Hydrogen Energ.*, 2022, **47**, 10175-10193.

4 S. D. Guan, T. S. Wang, X. L. Fu, L. Z. Fan, Z. J. Peng, *Appl. Surf. Sci.*, 2020, **508**, 145241.

5 Y. Zhou, Z. J. Yao, H. L. Zhang, X. X. Zhang, Q. X. Jia, S. S. Song, J. J. Sun, M. L. Qi, Y. F. Yang, *J. Colloid Interf. Sci.*, 2025, **694**, 137699.

6 J. J. Wang, X. Y. Yue, Z. Liu, Z. K. Xie, Q. Zhao, A. Abudula, G. Q. Guan, *J. Colloid Interf. Sci.*, 2022, **625**, 248-256.

7 D. W. Cao, W. D. Fan, W. P. Kang, Y. Y. Wang, K. A. Sun, J. C. Zhao, Z. Y. Xiao, D, F. Sun, *Mater. Today Energy*, 2019, **12**, 53-61.

8 S. C. Wang, S. B. Xie, M. Zhang, Y. J. Jiang, H. W. Luo, J. Tang, F. H. Zheng, Q. Y. Li, H. Q. Wang, Q. C. Pan, *J. Colloid Interf. Sci.*, 2024, **663**, 387-395.

9 H. P. Zhou, Y. B. Zhang, Y. J. Cao, X. W. Zhou, *Mater. Lett.*, 2019, **238**, 222-225.

10 S. Y. Wan, Q. M. Liu, H. Y. Chen, H. J. Zhu, Y. L. Wang, S. Y. Cao, *J. Power Sources*, 2022, **542**, 231804.

11 F. S. Zhu, S. Y. Zhang, Q. F. Zhang, K. J. Ma, J. Wu, Y. R. Cai, *Electrochim. Acta*, 2025, **510**, 145383.